Pr- and La-doping effects on the magnetic anisotropy in the antiferromagnetic phase of Kondo semiconductor $CeRu_2Al_{10}$

K. Yoshida,[1] R. Okubo,[1] H. Tanida,[1] T. Matsumura,[1] M. Sera,[1] T. Nishioka,[2] M. Matsumura,[2] C. Moriyoshi,[3] and Y. Kuroiwa[3]

[1]*Department of ADSM, Hiroshima University, Higashi-Hiroshima 739-8530, Japan*

[2]*Graduate School of Integrated Arts and Sciences, Kochi University, Kochi 780-8520, Japan*

[3]*Department of Physics, Hiroshima University, Higashi-Hiroshima 739-8530, Japan*

(Received 6 April 2015; revised manuscript received 19 May 2015; published 12 June 2015)

We have studied the Pr- and La-doping effects on the magnetic anisotropy in the antiferro-magnetic (AFM) phase of $CeRu_2Al_{10}$. The crystalline electric field (CEF) splitting in $PrRu_2Al_{10}$ was found to be as large as ~800 K with a singlet ground state. In $Ce_{1-x}Pr_xRu_2Al_{10}$, the CEF level scheme of the Pr ion is not changed with x. The AFM moment (m_{AF}) is rotated from c to b axis in both systems at $x_c^{sr} \sim 0.03$ and ~0.07 for Ln=Pr and La, respectively. As the ionic radius of La and Pr is larger and smaller than that of Ce, respectively, these results indicate that the chemical pressure effect is not associated with the rotation of m_{AF}, but is caused by the suppression of the c-f hybridization originating from the decrease of $4f$ electrons of Ce ions by Ce-site substitution. Since a small amount of Pr or La doping changes easily the magnetization easy axis of all the moments on Ce sites, the origin of the magnetic anisotropy is not the local single ion effect but the bandlike effect through the anisotropic c-f hybridization. The magnetic phase diagrams of $Ce_{1-x}Ln_xRu_2Al_{10}$ indicate that above x_c^{sr}, the AFM order with $m_{AF} \parallel b$ continues to exist up to x_c, which is ~0.4 and ~0.6 in Ln=Pr and Ln=La, respectively. This indicates that even in the sample with an AFM transition temperature (T_0) near x_c, the anisotropic c-f hybridization dominates the AFM order. A large positive transverse magnetoresistance is seen below T_0, but a very small one above T_0. Together with the results of Hall resistivity and the observation of Shubnikov–de Haas oscillation, we propose that there exist large Fermi surfaces above T_0 and small ones below T_0. A gap is opened by the AFM order on almost the area of the large Fermi surface, and small Fermi surfaces are constructed below T_0, although we do not know the mechanism, which might be specific to the AFM order in Kondo semiconductors. The largest suppression of the magnetic scattering below T_0 is observed for the current $I \parallel a$ and the smallest one for $I \parallel b$. This anisotropy may be associated with the anisotropic c-f hybridization, which may contribute to the anisotropic magnetic scattering of the conduction electron below T_0.

DOI: 10.1103/PhysRevB.91.235124 PACS number(s): 75.30.Et, 75.30.Gw

I. INTRODUCTION

The Kondo semiconductors CeT_2Al_{10} (T=Ru, Os) with orthorhombic $YbFe_2Al_{10}$-type structure (space group $Cmcm$) [1] have attracted considerable interest because of their unusual properties in the antiferro-magnetic (AFM) ordered phase. These compounds are the first examples of the AFM-Kondo semiconductor. The AFM order in this system has the following characteristics. (1) High transition temperature T_0 of 27 K, which is much higher than $T_N = 17$ K of GdT_2Al_{10} [2–5]. (2) $CeRu_2Al_{10}$ is located at the boundary between the localized and itinerant regime, from the rapid increase of T_0 by a small pressure and the change into the intermediate valence regime with a larger pressure [3,6–14]. (3) A spin-singlet-like characteristic is seen in χ_a and the magnetization curve for $H \parallel a$. Although χ_a is perpendicular magnetic susceptibility, a large decrease is seen below T_0 and a pronounced concave magnetization curve is seen for $H \parallel a$ in the AFM phase [15–20]. (4) The direction of the AFM moment m_{AF} is along the c axis, regardless of the large single-ion magnetic anisotropy of $\chi_a \gg \chi_c \gg \chi_b$ above T_0 [21–26]. Here, χ_a is the magnetic susceptibility along the a axis, etc. As its origin, we proposed that the strong c-f hybridization along the a axis avoids m_{AF} to align along the a axis [16]. Furthermore, m_{AF} is easily rotated from c to b or from c to a axis by a small magnetic field, a small amount of Ce- or Ru-site substitution and pressure, etc. [27–40]. (5) The spin gap and also charge gap appear in the AFM-ordered phase, whose origin has not yet been clarified [6,40–53]. (6) The anisotropic shrinkage of the lattice constants from the normal lanthanide contraction is seen in the a and c axes but not in the b axis, indicating the importance of the anisotropic c-f hybridization. There, the two-dimensional electronic structure is suggested [54–56]. (7) The large crystalline electric field (CEF) splitting Δ_{CEF} in Ce- and Yb-based compounds among LnT_2Al_{10}. The origin of the large Δ_{CEF} in CeT_2Al_{10} was ascribed to the large c-f hybridization [1,31,55–59]. (8) The ground state of $CeRu_2Al_{10}$ is metallic, with small Fermi surfaces [60–62].

The doping effects in $CeRu_2Al_{10}$ have been investigated extensively [15,17,32–40,44,46,47,55]. The doping effects often provide unexpected results, especially in the magnetic anisotropy in the AFM phase. One must clarify the origin of the unusual magnetic anisotropy in the AFM phase in order to understand the microscopic mechanism of the AFM order in the Kondo semiconductor $CeRu_2Al_{10}$.

In our previous paper [32], we reported that m_{AF} is easily rotated from c to b axis by a small amount of La doping. This rotation appears at $x \sim 0.07$ in $Ce_{1-x}La_xRu_2Al_{10}$. In $Ce_{0.9}La_{0.1}Ru_2Al_{10}$, the AFM order with $m_{AF} \parallel b$ is realized at the ambient pressure but m_{AF} is easily rotated from b to c axis by a small magnitude of pressure. $m_{AF} \parallel b$ at the ambient pressure was directly confirmed by the neutron diffraction experiment [40]. This clearly indicates that the enhancement of the c-f hybridization makes the AFM order with $m_{AF} \parallel c$ more stable than that with $m_{AF} \parallel b$. Thus, as the origin of the rotation

of m_{AF} from c to b axis by La doping at the ambient pressure, we proposed the reduction of the c-f hybridization due to the negative chemical pressure induced by La doping whose ionic radius is larger than that in the Ce ion. Very recently, it was reported that in Re-doped $CeRu_2Al_{10}$, the rotation of m_{AF} from c to b axis is induced and in Re-doped $CeOs_2Al_{10}$, the direction of m_{AF} is maintained along the c axis, with a reduced magnitude of m_{AF} [39]. In $Ce_{0.9}La_{0.1}Os_2Al_{10}$, $m_{AF} \parallel c$ is still maintained [40]. These results are difficult to understand simply by the variation of the c-f hybridization due to Re doping, because Re doping was considered to enhance the c-f hybridization and have a tendency to change the system into the intermediate valence regime. Thus, the magnetic anisotropy in the AFM phase in CeT_2Al_{10} seems to be not so simple. Up to now, the doping effects have been studied mainly by nonmagnetic ions. To get more information on the magnetic anisotropy, it is interesting to investigate the doping effects also by magnetic ions.

As for the CEF splitting in LnT_2Al_{10}, it was suggested that Δ_{CEF} is small except in Ce- and Yb-based compounds [56], from the temperature dependence of the magnetic susceptibility of LnT_2Al_{10} [1]. On the other hand, the detailed investigation of the CEF level scheme in localized systems was scarcely investigated. For NdT_2Al_{10}, rather detailed studies were performed and Δ_{CEF} was estimated to be $\sim$300 K [31,55,59]. More detailed investigations are necessary to obtain the systematic change of the CEF level scheme in LnT_2Al_{10} using single crystals.

In the present paper, first, we investigated the CEF level scheme in $PrRu_2Al_{10}$ using the single crystal because although the CEF ground state was found to be singlet, the CEF level scheme was considered to be small from the results of the polycrystal and not oriented single crystal [1,4,63]. Second, we investigated the Pr-doping effect on the magnetic properties in $Ce_{1-x}Pr_xRu_2Al_{10}$ focusing on the effect on the CEF level scheme and magnetic anisotropy in the AFM phase. Third, we compared the transport properties of $Ce_{1-x}Pr_xRu_2Al_{10}$ with those of $Ce_{1-x}La_xRu_2Al_{10}$ to examine the scattering mechanism of the conduction electron in the AFM phase.

II. EXPERIMENTAL

The single crystals of $Ce_{1-x}Pr_xRu_2Al_{10}$ and $Ce_{1-x}La_xRu_2Al_{10}$ were grown by Al self-flux method. The specific heat and magnetic susceptibility were measured by PPMS and MPMS (Quantum Design), respectively. The electrical resistivity was measured by the usual four-probe ac method in magnetic field up to 14.5 T. The lattice parameters of $Ce_{1-x}La_xRu_2Al_{10}$ were determined by a high-energy synchrotron powder diffraction experiment at room temperature at BL02B2 in SPring-8 using the large Debye-Sherrer camera equipped with an imaging plate as a two-dimensional detector. High-energy x rays with wavelength $\lambda = 0.66823$ Å were used as incident x rays.

III. EXPERIMENTAL RESULTS

A. $PrRu_2Al_{10}$

The temperature dependencies of the magnetic susceptibility χ of $PrRu_2Al_{10}$ along the three crystal axes are shown in Fig. 1(a). The relation of $\chi_a > \chi_c > \chi_b$ is the same as that in the localized NdT_2Al_{10} (T=Ru, Os, Fe) [31,55]. In NdT_2Al_{10}, the anisotropy of χ appears below $\sim$150 K indicating a small CEF splitting. On the other hand, in $PrRu_2Al_{10}$, the anisotropy of χ appears below $\sim$300 K, where χ_b is much smaller than χ_a and χ_c. This suggests the large CEF splitting in $PrRu_2Al_{10}$. χ_a and χ_c show a Curie-Weiss behavior at high temperatures but show a saturated behavior below $\sim$20 K. χ_b shows a broad maximum at $\sim$60 K and is independent of the temperature below $\sim$20 K. These indicate that the CEF ground state in $PrRu_2Al_{10}$ is a singlet and the first excited CEF state is located at $\sim$80 K above the ground state. We analyzed the results of χ by using the following CEF Hamiltonian,

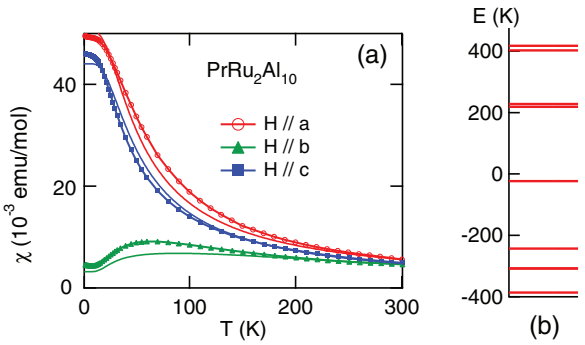

FIG. 1. (Color online) (a) Temperature dependence of the magnetic susceptibility of $PrRu_2Al_{10}$ in magnetic fields along the a, b, and c axes measured at $H = 0.1$ T and (b) the crystalline electric field (CEF) level scheme obtained by the CEF calculation. Solid lines in (a) indicate the calculated results obtained by the CEF calculation. See text for details.

$$\mathcal{H} = B_2^0 O_2^0 + B_2^2 O_2^2 + B_4^0 O_4^0 + B_4^2 O_4^2 + B_4^4 O_4^4 + B_6^0 O_6^0 + B_6^2 O_6^2 + B_6^4 O_6^4 + B_6^6 O_6^6. \quad (1)$$

Here, the quantization axis is taken as the c axis. The solid three lines in Fig. 1(a) are the calculated results by using the CEF parameters of $(B_2^0, B_2^2, B_4^0, B_4^2, B_4^4, B_6^0, B_6^2, B_6^4, B_6^6) =$ (5.0, −0.1095, 0.27, −0.74844, 0.3675, 0, 0.003, 0.005, 0) K. The experimental results could be reproduced well by the calculation. The CEF level scheme is shown in Fig. 1(b), which is denoted by (418.01, 402.81, 227.59, 218.70, −23.04, −242.95, −307.77, −307.98, −395.38) K. The CEF ground state is a singlet and the first excited state is located at $\sim$87 K above the ground state. The overall CEF splitting Δ_{CEF} is as large as $\sim$800 K. This value is much larger than $\sim$300 K in the localized $NdRu_2Al_{10}$ [31,59] and even larger than 540 K in $CeRu_2Al_{10}$ [57]. The origin of a large CEF splitting is not known at present. Here, we should note that the above CEF level scheme is one of the multiple solutions to reproduce the magnetic susceptibility. The inelastic neutron scattering experiments are necessary to obtain the secure CEF level scheme.

Figure 2(a) shows the temperature dependence of the specific heat C of $PrRu_2Al_{10}$ and $LaRu_2Al_{10}$ in the form of C/T. That of $LaRu_2Al_{10}$ shows a normal behavior as is seen in nonmagnetic compounds. On the other hand, in $PrRu_2Al_{10}$, a broad but clear hump is seen at $\sim$20 K. The magnetic specific heat C_{mag} of $PrRu_2Al_{10}$ is shown in the form of C_{mag}/T in

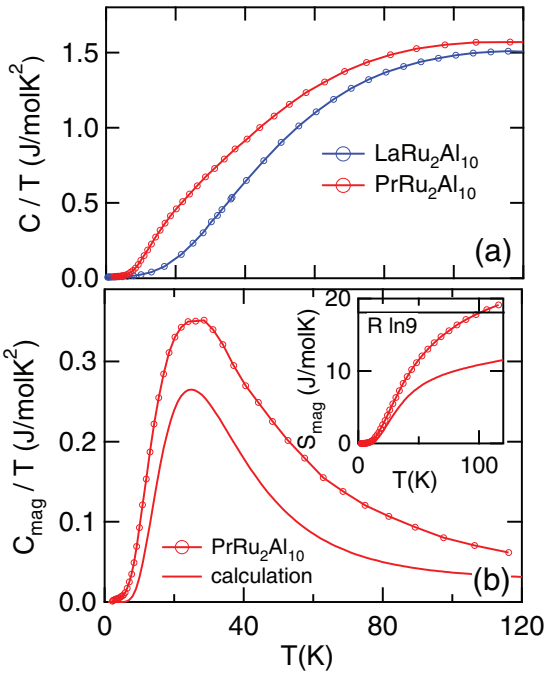

FIG. 2. (Color online) (a) Temperature dependence of the specific heat of $PrRu_2Al_{10}$ and $LaRu_2Al_{10}$ in the form of C/T. (b) Temperature dependence of the magnetic specific heat of $PrRu_2Al_{10}$ in the form of C_{mag}/T. The solid red line indicates the result obtained by the CEF calculation. The inset of (b) indicates the temperature dependence of the magnetic entropy of $PrRu_2Al_{10}$ and the solid red line indicates the calculated result.

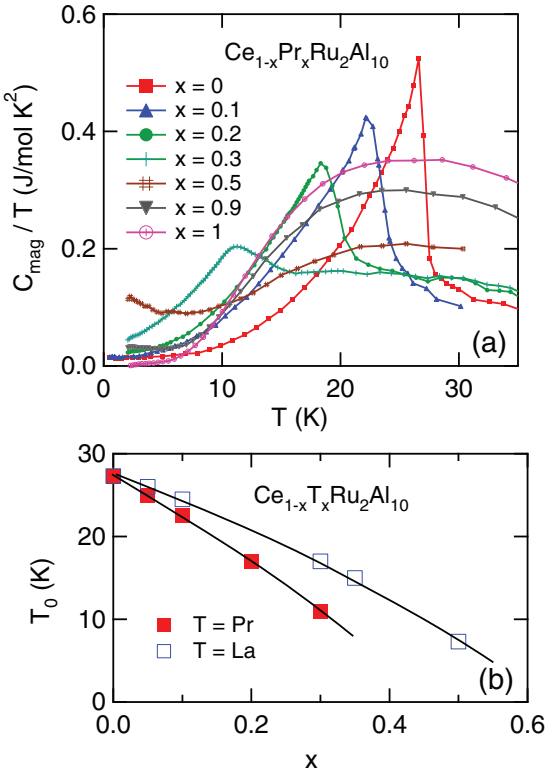

FIG. 3. (Color online) (a) Specific heat of $Ce_{1-x}Pr_xRu_2Al_{10}$ in the form of C_{mag}/T. (b) x dependence of the AFM transition temperature T_0 of $Ce_{1-x}Pr_xRu_2Al_{10}$ and $Ce_{1-x}La_xRu_2Al_{10}$ [15].

Fig. 2(b). This clearly shows the existence of a Schottky peak at ∼25 K, while it is difficult to obtain the information on the overall CEF splitting from the present result below 120 K. Here, C_{mag} is obtained by subtracting simply the specific heat of $LaRu_2Al_{10}$ as a phonon contribution. The red solid line is the calculated temperature dependence of C_{mag}/T obtained by using the CEF level scheme shown in Fig. 1(b). Although the characteristic temperature dependence of the experimental result could be reproduced by the calculation, the magnitude of the experimental result is rather large compared with the calculated one. The former indicates that the CEF level scheme obtained by the fitting in a low-energy region is correct but the latter indicates that the phonon specific heat is different between $PrRu_2Al_{10}$ and $LaRu_2Al_{10}$. This is also seen in the temperature dependence of the magnetic entropy S_{mag}, which is shown in the inset in Fig. 2(b). Although S_{mag} is expected to saturate to $R \ln 9$ at ∼800 K, the experimental result shows that S_{mag} exceeds the saturated value of $R \ln 9$ already at 100 K. Thus, the specific heat of $LaRu_2Al_{10}$ could not be used as the phonon contribution in $PrRu_2Al_{10}$.

B. $Ce_{1-x}Pr_xRu_2Al_{10}$

1. Specific heat

Figure 3(a) shows the temperature dependence of the specific heat of $Ce_{1-x}Pr_xRu_2Al_{10}$ in the form of C_{mag}/T. In all the compounds, C_{mag} is obtained simply by subtracting the specific heat of $LaRu_2Al_{10}$. In $CeRu_2Al_{10}$, a sharp peak is seen at T_0 and the $e^{-\Delta_{SG}/T}$ dependence is seen at low temperatures, which indicates the existence of the gap in the magnetic excitation spectrum. Δ_{SG} is the magnitude of the spin gap. In $Ce_{1-x}Pr_xRu_2Al_{10}$, a rather sharp peak is seen at T_0 up to $x = 0.2$. In $Ce_{0.7}Pr_{0.3}Ru_2Al_{10}$, a broad peak is seen at $T_0 \sim 11$ K and also a broad hump is recognized at ∼25 K. The latter originates from the Schottky-type specific heat due to the CEF splitting of the Pr ion. In $Ce_{0.5}Pr_{0.5}Ru_2Al_{10}$, a broad maximum is more clearly seen at ∼25 K. At low temperatures, the AFM order disappears and in place, the increase of C_{mag}/T is seen below ∼7 K. In $Ce_{0.1}Pr_{0.9}Ru_2Al_{10}$, roughly the same temperature dependence as in $PrRu_2Al_{10}$ is seen at high temperatures and a small increase of C_{mag}/T is seen below ∼7 K, which indicates the formation of the impurity Kondo state on the Ce ion.

Figure 3(b) shows the x dependence of T_0 in $Ce_{1-x}Pr_xRu_2Al_{10}$ and $Ce_{1-x}La_xRu_2Al_{10}$. T_0 decreases with increasing x and may disappear at $x_c \sim 0.4$ in $Ce_{1-x}Pr_xRu_2Al_{10}$ and at $x_c \sim 0.6$ in $Ce_{1-x}La_xRu_2Al_{10}$. The critical x_c value is larger in $Ce_{1-x}La_xRu_2Al_{10}$ than in $Ce_{1-x}Pr_xRu_2Al_{10}$. This difference might be because the Pr ion is magnetic, although the CEF ground state is the singlet. The Van Vleck term from the first excited state, located ∼77 K above the ground state, may contribute to the more rapid suppression of T_0. We note that in $Ce_{0.5}La_{0.5}Ru_2Al_{10}$, the peak of C/T is located at ∼5 K [15] but that of C is located at ∼7 K. In Fig. 3(b), this temperature of ∼7 K is plotted. This temperature of ∼7 K is consistent with T_0 estimated by the electrical resistivity, which will be shown later.

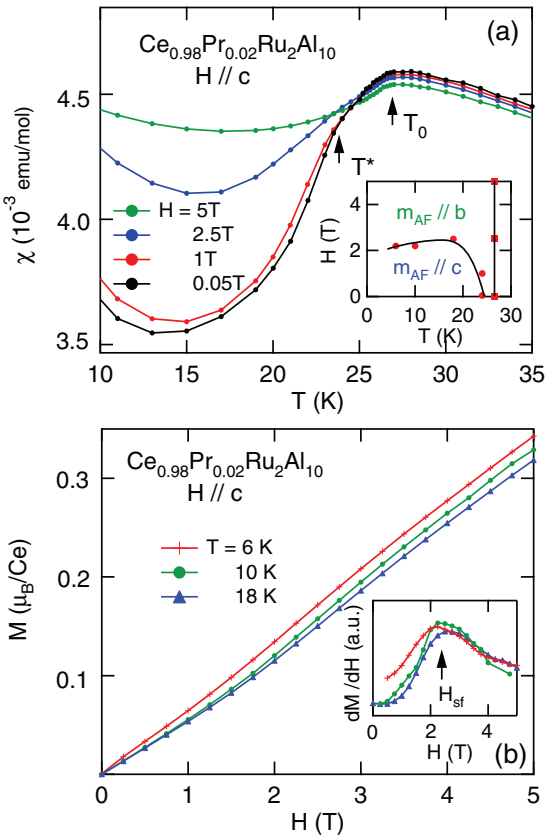

FIG. 4. (Color online) (a) Temperature dependence of the magnetic susceptibility and (b) magnetization curve of $Ce_{0.98}Pr_{0.02}Ru_2Al_{10}$ along the c axis. The insets in (a) and (b) show the magnetic phase diagram for $H \parallel c$ and the magnetic field dependence of dM/dH, respectively.

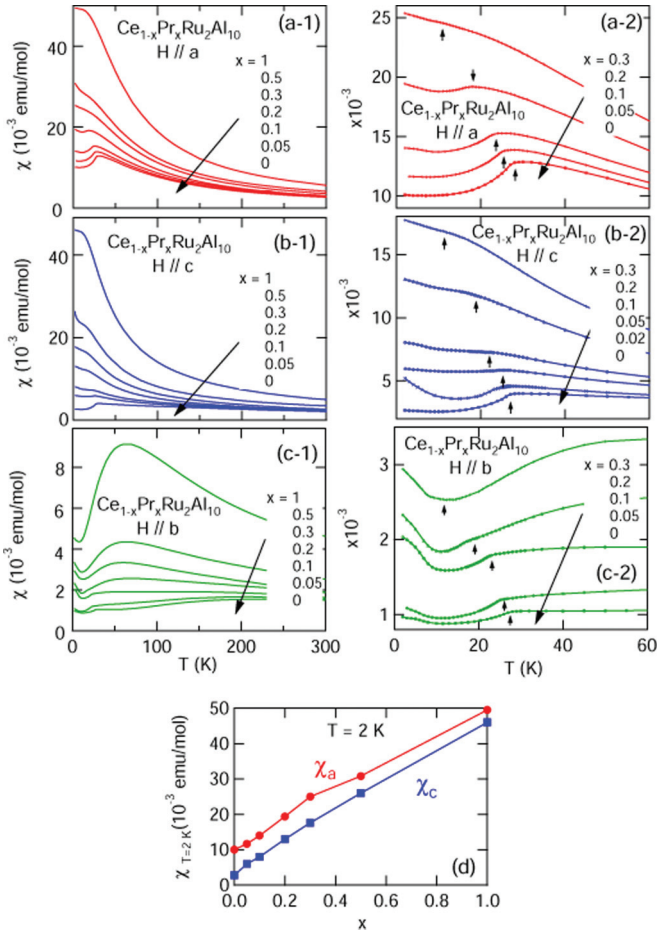

FIG. 5. (Color online) Temperature dependence of the magnetic susceptibility of $Ce_{1-x}Pr_xRu_2Al_{10}$ for (a-1) $H \parallel a$, (b-1) $H \parallel b$, and (c-1) $H \parallel c$. (a-2), (b-2), and (c-2) show those in an expanded scale below 60 K. (d) x dependence of the magnitude of χ_a and χ_c of $Ce_{1-x}Pr_xRu_2Al_{10}$ at $T = 2$ K.

2. *Magnetic susceptibility*

First, we show the magnetic properties of $Ce_{0.98}Pr_{0.02}Ru_2Al_{10}$. Figures 4(a) and 4(b) show the temperature dependence of χ_c and the magnetization curves of $Ce_{0.98}Pr_{0.02}Ru_2Al_{10}$ for $H \parallel c$, respectively. $T_0 = 27$ K corresponding to the peak temperature of χ_c and $T^* = 24$ K below which a sharp decrease is seen with decreasing temperature. We note that these results are very similar to those in $Ce_{0.95}La_{0.05}Ru_2Al_{10}$ [32] and $m_{AF} \parallel b$ is realized above H_{sf} in $CeRu_2Al_{10}$ [30]. Thus, the AFM order with $m_{AF} \parallel c$ is realized below T^* and that with $m_{AF} \parallel b$ between T^* and T_0. In the magnetization curves shown in Fig. 4(b), an anomaly is seen at $H_{sf} \sim 2$ T, originating from the spin-flop transition from $m_{AF} \parallel c$ to $m_{AF} \parallel b$. The magnetic phase diagram for $H \parallel c$ shown in the inset of Fig. 4(a) indicates that the AFM order with $m_{AF} \parallel c$ is rapidly destabilized by a small amount of Pr doping and the ground state is changed to the AFM order with $m_{AF} \parallel b$ for $x > 0.03$ in $Ce_{1-x}Pr_xRu_2Al_{10}$, which will be shown later. A similar change of the AFM ground state is also seen in $Ce_{1-x}La_xRu_2Al_{10}$ at $x \sim 0.07$.

Figures 5(a-1)–5(c-1) show the temperature dependence of the magnetic susceptibility of $Ce_{1-x}Pr_xRu_2Al_{10}$ along the three crystal axes, and Figs. 5(a-2)–5(c-2) show those in the expanded scale at low temperatures. χ_a shows a large decrease below T_0 in $CeRu_2Al_{10}$, although the AFM order with $m_{AF} \parallel c$ is realized. This decrease is still recognized at $x = 0.2$. A drastic change appears in the temperature dependence of χ_c between $x = 0.02$ and 0.05. Also in χ_b, a pronounced change is observed at $x = 0.05$. Although a small decrease below T_0 is seen in χ_b in $CeRu_2Al_{10}$, its decrease is larger and clearer for $x = 0.05$. This change in χ_b is accompanied with the disappearance of the decrease of χ_c below T_0. These results indicate that the rotation of m_{AF} from c to b axis appears between $x = 0.02$ and 0.05. On the other hand, in χ_a, roughly the same temperature dependence is seen between $x = 0$ and 0.05. The decrease of χ_b below T_0 is clearly seen also for $x = 0.1$, although a clear anomaly is not seen in χ_a and χ_c. From these results, we conclude that the AFM order with $m_{AF} \parallel b$ is realized up to $x = 0.3$, which is more strongly supported by the results of the magnetoresistance as will be shown later. Figure 5(d) shows the x dependence of the magnitudes of χ_a and χ_c at $T = 2$ K, which increase with increasing x roughly proportional to x. This strongly suggests that the Pr ion behaves as nearly a free magnetic ion and a single ion nature is maintained in $Ce_{1-x}Pr_xRu_2Al_{10}$. A similar x dependence is also seen in χ_b if we take the value at ~60 K.

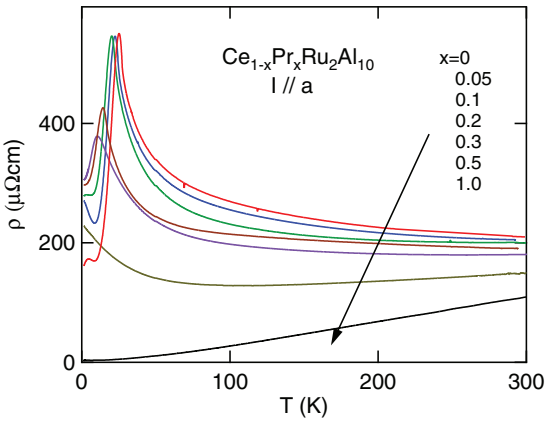

FIG. 6. (Color online) Temperature dependence of the electrical resistivity of $Ce_{1-x}Pr_xRu_2Al_{10}$ ($x = 0$, 0.05, 0.1, 0.2, 0.3, 0.5, 1.0) for $I \parallel a$.

3. *Electrical resistivity*

Figure 6 shows the temperature dependence of the electrical resistivity ρ of $Ce_{1-x}Pr_xRu_2Al_{10}$ in zero magnetic field. The electrical current I flows along the a axis. The results are very similar to those in $Ce_{1-x}La_xRu_2Al_{10}$, which will be shown later. This indicates that the magnetic scattering by Pr ions is very small, which may be due to the singlet CEF ground state formed at low temperatures and a large CEF splitting at high temperatures. The semiconducting behavior is suppressed with increasing x and is changed to the single-impurity Kondo-like behavior in a large-x region. ρ of $PrRu_2Al_{10}$ shows the normal metal-like behavior and a small anisotropy depending on the current direction, while they are not shown here. The residual resistivity ratio RRR is as large as 32, indicating the good quality of the sample.

Figures 7(a)–7(c) show the temperature dependence of ρ of $Ce_{1-x}Pr_xRu_2Al_{10}$ below 40 K, for $I \parallel a, b$, and c, respectively. The increase of ρ below T_0 is small for $I \parallel a$ and is large for $I \parallel b$ and c. This tendency is clearly seen at least up to $x = 0.1$. A kink at T_0 for $x > 0.2$ is very broad. ρ shows a rapid decrease below T_{max}, where ρ exhibits a broad maximum a few kelvins below T_0 for all the current directions. For $x = 0.3$, although the decrease of ρ below T_0 is seen for $I \parallel a$ and c, it is not seen for $I \parallel b$. For $x = 0.5$, ρ shows the single-impurity Kondo-like behavior. Here, we should note that the resistance minimum is

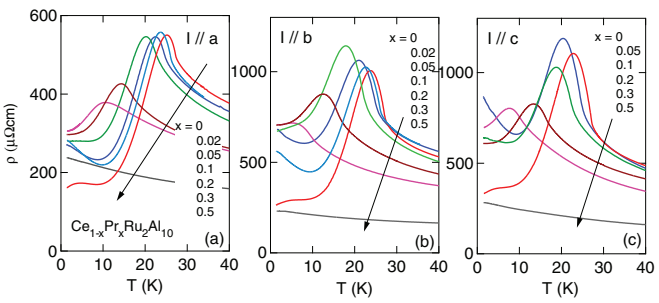

FIG. 7. (Color online) Temperature dependence of the electrical resistivity of $Ce_{1-x}Pr_xRu_2Al_{10}$ below $T = 40$ K for (a) $I \parallel a$, (b) $I \parallel b$, and (c) $I \parallel c$.

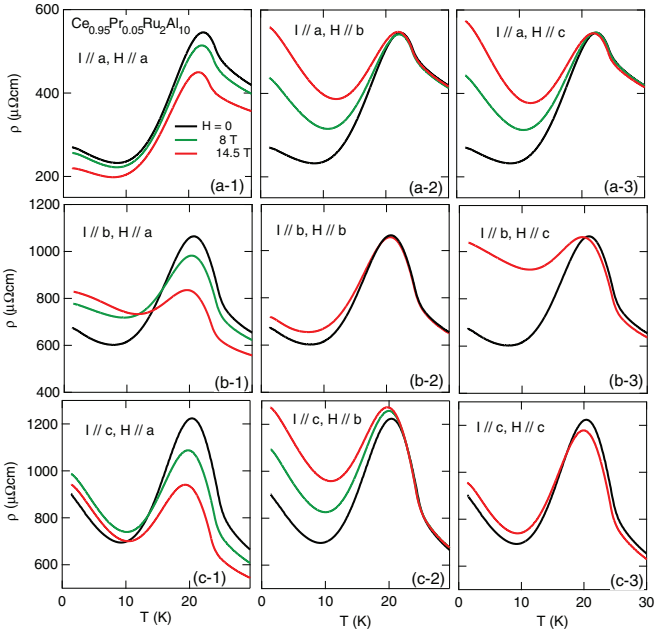

FIG. 8. (Color online) Temperature dependence of the electrical resistivity of $Ce_{0.95}Pr_{0.05}Ru_2Al_{10}$ under both longitudinal and transverse magnetic fields. (a-1)–(a-3) $I \parallel a$, (b-1)–(b-3) $I \parallel b$, and (c-1)–(c-3) $I \parallel c$. (-1), (-2), and (-3) indicate $H \parallel a$, b, and c, respectively. Black, green, and red colors are for $H = 0$, 8 T, and 14.5 T, respectively.

seen at $T_{min} \sim 10$ K for $x = 0.02 \sim 0.05$ and does not exist for $x > 0.1$. The increase of ρ below T_{min} is largest for $I \parallel c$. A similar temperature dependence of ρ accompanied with T_{min} is observed also in the La-doped sample with $x = 0.05$, which will be shown later. Since this increase is induced by only 2% doping of the Pr ion, the magnetic impurity effect on the Fermi liquid ground state such as the Kondo effect could be considered as the origin. In order to check whether this is due to the magnetic impurity effect such as a Kondo effect or not, we investigated the magnetoresistance in $Ce_{0.95}Pr_{0.05}Ru_2Al_{10}$ in detail. The negative magnetoresistance is expected if it is due to the magnetic impurity effect such as a Kondo effect.

Figures 8(a-1)–8(c-3) show the temperature dependence of ρ of $Ce_{0.95}Pr_{0.05}Ru_2Al_{10}$ in magnetic fields parallel to the a, b, and c axes, respectively. The large positive magnetoresistance is observed under the transverse magnetic field in all the cases. Under the longitudinal magnetic field, ρ_a shows a small negative magnetoresistance below T_{min}, and ρ_b and ρ_c show a small positive one. These indicate that the increase of ρ below T_{min} is robust against the magnetic field. This rules out the possibility such as an impurity Kondo effect. Further studies are necessary to clarify the origin of the resistance minimum. We note that a Shubnikov–de Haas (SdH) oscillation is observed in this sample, as in $Ce_{0.95}La_{0.05}Ru_2Al_{10}$, which will be shown later. For $H \parallel a$, a negative magnetoresistance is observed at high temperatures for all the current directions. However, below $\sim$15 K, it becomes small for $I \parallel a$ and is changed to a positive magnetoresistance for $I \parallel b$ and c, which is due to the transverse magnetoresistance. The largest negative magnetoresistance appears at T_{max}. For $H \parallel b$ and c, a longitudinal magnetic field effect is small. For $H \parallel b$ and

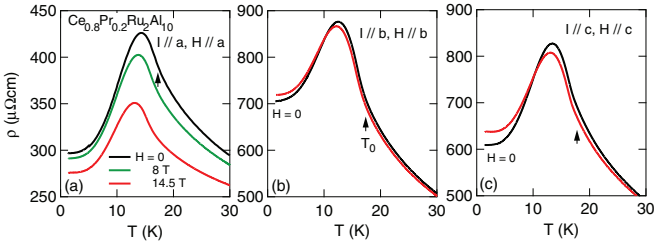

FIG. 9. (Color online) Temperature dependence of the electrical resistivity of $Ce_{0.8}Pr_{0.2}Ru_2Al_{10}$ under the longitudinal magnetic field along the three crystal axes. (a) $I, H \parallel a$, (b) $I, H \parallel b$, and (c) $I, H \parallel c$. T_0 is shown by the arrow. Black, green, and red colors are for $H = 0$, 8 T, and 14.5 T, respectively.

c, a very small transverse magnetic field effect is seen above T_{max} but a large negative one is seen below T_{max}.

Figures 9(a)–9(c) show the temperature dependence of ρ of $Ce_{0.8}Pr_{0.2}Ru_2Al_{10}$ under the longitudinal magnetic fields along the three crystal axes. The anomaly at T_0 is much broader than that for $x < 0.1$. The decrease of ρ below T_{max} is anisotropic, i.e., largest for $I \parallel a$ and smallest for $I \parallel b$. This tendency is much more enhanced for $x = 0.3$, which will be shown below. A large negative magnetoresistance is seen for $I \parallel a$ under $H \parallel a$ in a wide temperature region. We note that the magnitude of the negative magnetoresistance is largest at T_{max} but is reduced with decreasing temperature. For $H \parallel b$ and c, the magnetic field effect is very small above T_{max} and a small positive one below T_{max}.

Figures 10(a-1)–10(c-3) show the temperature dependence of ρ of $Ce_{0.7}Pr_{0.3}Ru_2Al_{10}$ in magnetic fields along the three crystal axes. The anomaly at T_0 in zero magnetic field is much broader than that for $x = 0.2$. For $I \parallel a$, it is difficult to distinguish between T_0 and T_{max}, while for $I \parallel b$ and c, T_0 could be recognized. A big difference depending on the current direction is seen in the temperature dependence of ρ below T_{max}. Below T_{max}, although the decrease is seen in ρ_a and ρ_c, ρ_b is almost constant below T_{max}. This strongly suggests the importance of the two-dimensional nature in the ac plane on the transport property. We should note that the magnitude of the decrease of ρ below T_{max} in zero magnetic field is much larger for $I \parallel a$ than for $I \parallel c$. It is ∼20% for $I \parallel a$ and ∼13% for $I \parallel c$. Such an anisotropic decrease of ρ below T_{max} is also seen in $Ce_{1-x}Pr_xRu_2Al_{10}$ ($x = 0.05$, 0.2) shown in Figs. 8 and 9. As for the magnetic field effect, it is small for $H \parallel b$ and c, but is large for $H \parallel a$. Under the transverse magnetic field of $H \parallel b$ and c, a positive magnetoresistance is seen below T_0 for $I \parallel a$ and c. For $H \parallel a$, a large negative magnetoresistance is seen for all the current directions. The magnitude of the negative magnetoresistance is largest at T_{max} and is reduced at lower temperatures. Figures 10(d) and 10(e) show the magnetoresistance of $Ce_{0.7}Pr_{0.3}Ru_2Al_{10}$ for $H \parallel a$ at $T = 1.4$ K and 10 K, respectively. Although at $T = 10$ K a large negative magnetoresistance is observed for all the current directions, an anisotropic behavior is seen at $T = 1.4$ K. The large negative magnetoresistance is seen for $I \parallel b$ and c, but it is small for $I \parallel a$. The latter is associated with the large decrease of ρ below T_{max} in zero magnetic field. Namely, as the magnetic scattering is already suppressed largely in zero

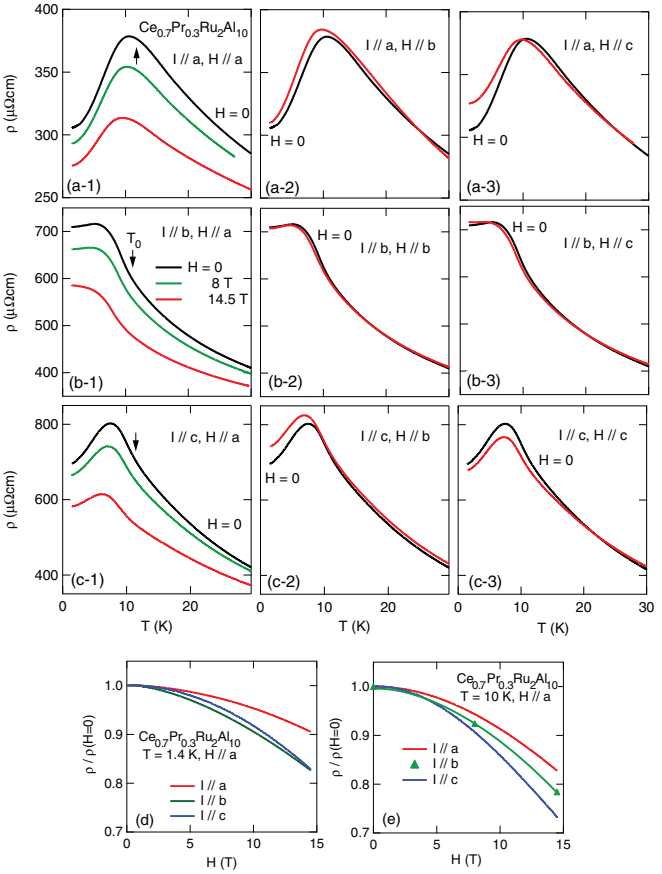

FIG. 10. (Color online) Temperature dependence of the electrical resistivity of $Ce_{0.7}Pr_{0.3}Ru_2Al_{10}$ under both longitudinal and transverse magnetic fields along the three crystal axes. (a-1)–(a-3) $I \parallel a$, (b-1)–(b-3) $H \parallel b$, and (c-1)–(c-3) $I \parallel c$. T_0 is shown by the arrow. (−1), (−2), and (−3) indicate $H \parallel a$, b, and c, respectively. Black, green, and red colors are for $H = 0$, 8 T, and 14.5 T, respectively. (d) and (e) show the magnetoresistance for $H \parallel a$ normalized by $\rho(H = 0)$ at $T = 1.4$ K and 10 K, respectively.

magnetic field at the lowest temperature, further suppression by magnetic field is small.

Figures 11(a)–11(c) show the temperature dependence of ρ of $Ce_{0.5}Pr_{0.5}Ru_2Al_{10}$ under the longitudinal magnetic fields along the three crystal axes. This compound does not show the magnetic order. In zero magnetic field, the Kondo-semiconductor-like behavior or the single-impurity Kondo-like behavior is seen in all the cases and the anisotropy

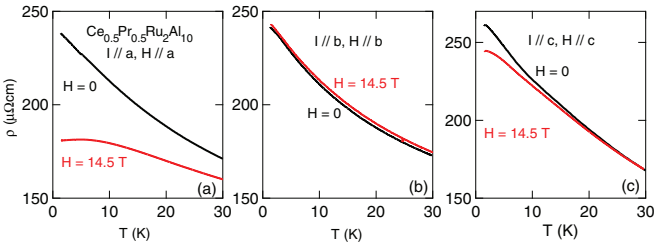

FIG. 11. (Color online) Temperature dependence of the electrical resistivity of $Ce_{0.5}Pr_{0.5}Ru_2Al_{10}$ under the longitudinal magnetic field along the three crystal axes. (a) $I, H \parallel a$, (b) $I, H \parallel b$, and (c) $I, H \parallel c$.

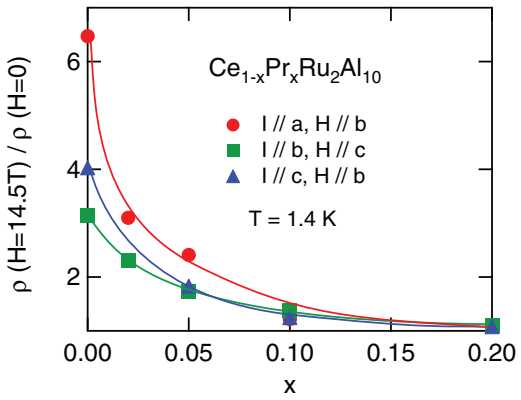

FIG. 12. (Color online) x dependence of the magnitude of the positive magnetoresistance at $T = 1.4$ K under the transverse magnetic field, which is in the form of $\rho(H = 14.5\,\mathrm{T})/\rho(H = 0)$ in $Ce_{1-x}Pr_xRu_2Al_{10}$. For $x = 0.02$ and 0.05, $\rho(H = 14.5$ T) at $T = 1.4$ K and $\rho(H = 0)$ at $T_{\min} \sim 10$ K are used to avoid the effect of the increase of ρ below $T_{\min}$.

of ρ is small. The magnitude of the negative magnetoresistance depending on the magnetic field direction seems to be associated with the relation of $\chi_a \gg \chi_c \gg \chi_b$ of Ce ions in the paramagnetic region.

Figure 12 shows the x dependence of the magnitude of the positive magnetoresistance in $Ce_{1-x}Pr_xRu_2Al_{10}$ at $T = 1.4$ K under the transverse magnetic field in the form of $\Delta\rho = \rho(H = 14.5\,\mathrm{T})/\rho(H = 0)$. The magnitude of $\Delta\rho$ reflects the quality of the sample. Namely, the better the sample quality, the larger $\Delta\rho$. Large $\Delta\rho$ in $CeRu_2Al_{10}$ is rapidly suppressed with increasing x. Here, we should note that regardless of such a large impurity scattering, the SdH oscillation is observed even for $x = 0.2$, which will be shown later. We also point out that the residual resistivity ρ_0 is not so much changed, although $\Delta\rho$ is rapidly suppressed.

Figures 13(a-1)–13(e-1) show the magnetoresistance of $Ce_{1-x}Pr_xRu_2Al_{10}$ at various temperatures, where ρ is normalized by $\rho(H = 0)$. Figures 13(a-2)–13(e-2) show the magnetic phase diagrams of these samples. The spin-flop transition from $m_{\mathrm{AF}} \parallel c$ to $m_{\mathrm{AF}} \parallel b$ is observed for $x = 0.02$ and that from $m_{\mathrm{AF}} \parallel c$ to $m_{\mathrm{AF}} \parallel b$ for $x = 0.05 \sim 0.3$. For the other magnetic field direction, no anomaly is seen up to 14.5 T in all the samples, while those are not shown here. From these results, we conclude that in zero magnetic field, m_{AF} is rotated from b to c axis at $x \sim 0.03$ in $Ce_{1-x}Pr_xRu_2Al_{10}$. With further increase of x, H_{sf} increases up to $x \sim 0.2$ and then decreases with increasing x towards $x_c \sim 0.4$. We note that ρ shows a broad but discontinuous increase for $x = 0.02$ or increase for $x = 0.05 \sim 0.3$ at H_{sf}. Namely, the value of ρ in the AFM phase with $m_{\mathrm{AF}} \parallel c$ is smaller than that in the AFM phase with $m_{\mathrm{AF}} \parallel b$. This indicates that the suppression of ρ by magnetic scattering is larger in the AFM state with a larger moment of $m_{\mathrm{AF}} \parallel c$ than that with a smaller moment of $m_{\mathrm{AF}} \parallel b$.

Figure 14 shows the x dependence of the spin-flop transition field H_{sf} of $Ce_{1-x}Pr_xRu_2Al_{10}$. H_{sf} from $m_{\mathrm{AF}} \parallel c$ to $\parallel b$ decreases with increasing Pr concentration and at $x_c^{\mathrm{sr}} \sim 0.03$, the magnetization easy axis in zero magnetic field changes from c to b axis. Here, x_c^{sr} is the critical x value where m_{AF}

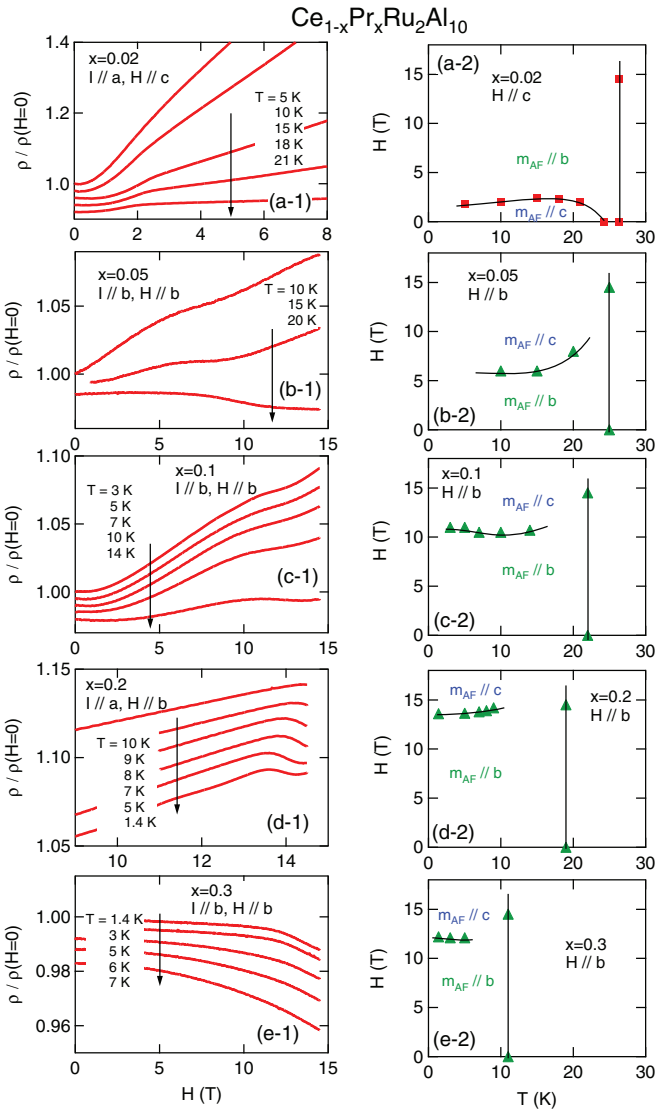

FIG. 13. (Color online) Magnetoresistance of $Ce_{1-x}Pr_xRu_2Al_{10}$: (a-1) $x = 0.02$, (b-1) $x = 0.05$, (c-1) $x = 0.1$, (d-1) $x = 0.2$, and (e-1) $x = 0.3$. Magnetic phase diagram of $Ce_{1-x}Pr_xRu_2Al_{10}$: (a-2) $x = 0.02$, (b-2) $x = 0.05$, (c-2) $x = 0.1$, (d-2) $x = 0.2$, and (e-2) $x = 0.3$. $H \parallel c$ for $x = 0.02$ and $H \parallel b$ for $x = 0.05$, 0.1, 0.2, and 0.3.

in the ground state rotates from c to b axis. H_{sf} from $m_{\mathrm{AF}} \parallel b$ to $\parallel c$ rapidly increases above $x_c^{\mathrm{sr}} \sim 0.03$ and after exhibiting a maximum at $x \sim 0.2$, it decreases towards $x_c \sim 0.4$ where the AFM order disappears. The present result indicates that at $x_c^{\mathrm{sr}} \sim 0.03$, the magnetic anisotropy in the bc plane disappears.

C. $Ce_{1-x}La_xRu_2Al_{10}$

1. Electrical resistivity

Figure 15 shows the temperature dependence of ρ of $Ce_{1-x}La_xRu_2Al_{10}$ for $I \parallel a$ in zero magnetic field. The results are very similar to those in $Ce_{1-x}Pr_xRu_2Al_{10}$. In $Ce_{0.5}La_{0.5}Ru_2Al_{10}$, there exists a maximum at $T_0 \sim 7$ K, while it does not exist in $Ce_{0.5}Pr_{0.5}Ru_2Al_{10}$. The former originates from the suppression of magnetic scattering below T_0 and the

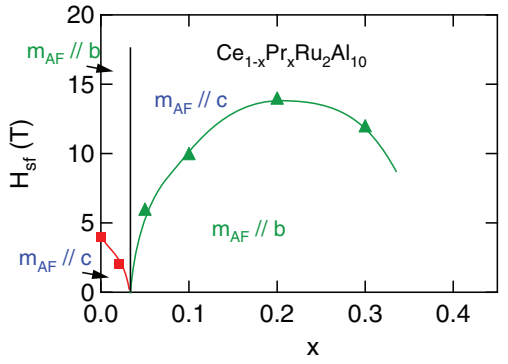

FIG. 14. (Color online) x dependence of the spin-flop transition field H_{sf} of $Ce_{1-x}Pr_xRu_2Al_{10}$. For $x < 0.03$, a spin-flop transition from $m_{AF} \parallel c$ to $\parallel b$ and for $x > 0.03$, that from $m_{AF} \parallel b$ to $\parallel c$. The solid vertical line at $x \sim 0.03$ is the boundary where the magnetic anisotropy in the bc plane is changed.

latter originates from no magnetic ordering down to very low temperature. ρ of $LaRu_2A_{10}$ shows a normal nonmagnetic behavior with $RRR \sim 18$. Its temperature dependence is similar to that of $PrRu_2Al_{10}$.

Figures 16(a-1)–16(b-4) show the temperature dependence of ρ of $Ce_{1-x}La_xRu_2Al_{10}$ normalized by ρ at $T = 30$ K in zero magnetic field for $I \parallel a$ and c. In Fig. 16, panels (a-3), (a-4), (b-1), and (b-2), the results in magnetic fields are also shown. Figure 16(c) shows the magnetoresistance of $Ce_{1-x}La_xRu_2Al_{10}$ ($x = 0.35$ and 0.5) for $H \parallel a$. Also in the present system, T_{min} appears at $x \sim 0.05$ at $T_{min} \sim 10$ K as is seen in $Ce_{1-x}Pr_xRu_2Al_{10}$. The similar anisotropic increase of ρ below T_{min} is seen as is observed in $Ce_{1-x}Pr_xRu_2Al_{10}$. The anomaly at T_0 for $I \parallel a$ is clearly seen up to $x = 0.1$ but is difficult to distinguish between T_0 and T_{max} for $x \geqslant 0.35$. For $I \parallel c$, the anomaly is clearly seen still for $x = 0.2$, different from a broad anomaly in $Ce_{0.8}Pr_{0.2}Ru_2Al_{10}$. As for the magnetic field effect, for $I \parallel a$ and $H \parallel a$, a negative magnetoresistance is seen. For $x = 0.35$, its magnitude is large above ~10 K but is reduced largely at low temperatures. For $x = 0.5$, the magnitude of negative magnetoresistance is large even at low temperatures, although the largest suppression of ρ at T_{max} is maintained.

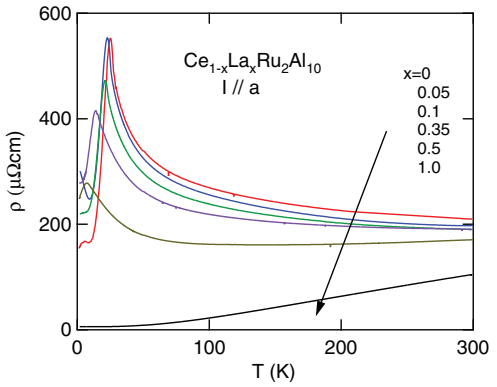

FIG. 15. (Color online) Temperature dependence of the electrical resistivity of $Ce_{1-x}La_xRu_2Al_{10}$ ($x = 0$, 0.05, 0.1, 0.35, 0.5, 1.0) for $I \parallel a$.

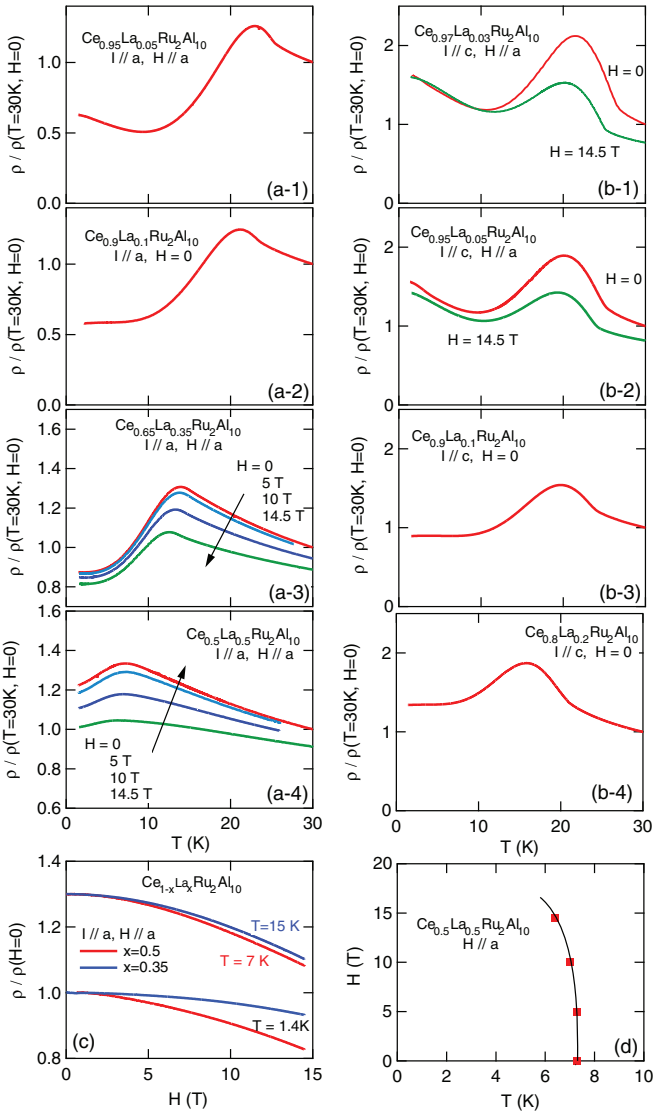

FIG. 16. (Color online) Temperature dependence of the electrical resistivity of $Ce_{1-x}La_xRu_2Al_{10}$ normalized by ρ at $T = 30$ K and $H = 0$ for $I \parallel a$: (a-1) $x = 0.05$, (a-2) $x = 0.1$, (a-3) $x = 0.35$, (a-4) $x = 0.5$; and for $I \parallel c$: (b-1) $x = 0.03$, (b-2) $x = 0.05$, (b-3) $x = 0.1$, (b-4) $x = 0.2$. In (a-3), (a-4), (b-1), and (b-2), those in magnetic fields are also shown. (c) Magnetoresistance for $x = 0.35$ and 0.5 at $T = 1.4$ K and ~10 K. $I \parallel a$ and $H \parallel a$. ρ is normalized by $\rho(H = 0)$ and the origin of the vertical axes of those at ~10 K are shifted by 0.3. (d) Magnetic phase diagram of $Ce_{0.5}La_{0.5}Ru_2Al_{10}$ for $H \parallel a$.

Although the temperature dependence of ρ in zero magnetic field in $Ce_{0.5}La_{0.5}Ru_2Al_{10}$ is similar to that in $Ce_{0.65}La_{0.35}Ru_2Al_{10}$, the magnetic field effect below T_0 is very different. As is seen in Fig. 16(c), a large negative magnetoresistance is seen at high temperatures around T_{max} in both samples. However, at $T = 1.4$ K, although a small negative magnetoresistance is seen for $x = 0.35$, a large one is seen for $x = 0.5$. This reflects the different nature of Ce ion in the AFM ground state between these two samples. For $x = 0.35$, the magnetic scattering is already suppressed largely at low temperatures in zero magnetic field. On the other hand, for $x = 0.5$, the Ce ion in the AFM ground

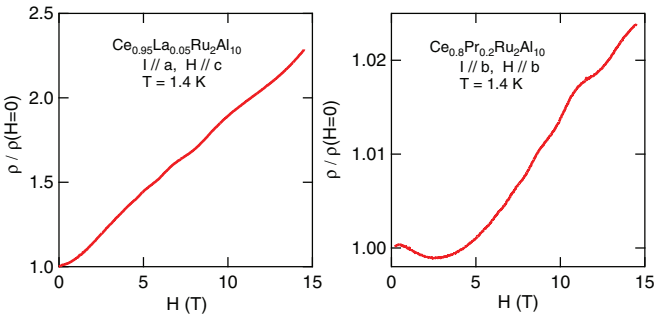

FIG. 17. (Color online) Shubnikov–de Haas oscillation of (a) $Ce_{0.95}La_{0.05}Ru_2Al_{10}$ and (b) $Ce_{0.8}Pr_{0.2}Ru_2Al_{10}$ at $T = 1.4$ K.

state has also a free-ion-like nature in the same way as in the paramagnetic region and so there exists a large negative magnetoresistance even at lowest temperature. For $I \parallel c$ and $H \parallel a$ shown in Figs. 16(b-1) and 16(b-2), although the large negative magnetoresistance is seen at high temperatures, a positive one at low temperatures is much more reduced than in $Ce_{0.95}Pr_{0.05}Ru_2Al_{10}$. Figure 16(d) shows the magnetic phase diagram of $Ce_{0.5}La_{0.5}Ru_2Al_{10}$ for $H \parallel a$. $T_0 \sim 7.3$ K and H_c is roughly estimated to be ~25 T. T_0 is about one fourth and H_c is one half of those of $CeRu_2Al_{10}$.

Figures 17(a) and 17(b) show the SdH oscillations of $Ce_{0.95}La_{0.05}Ru_2Al_{10}$ and $Ce_{0.8}Pr_{0.2}Ru_2Al_{10}$ at $T = 1.4$ K, respectively. The SdH frequency is ~22 T and ~43 T, respectively. These values are similar to that observed in $CeRu_2Al_{10}$ [60,62]. The observation of the SdH oscillation indicates the high quality of the sample. On the other hand, the scattering by doped Ln ions clearly increases as is seen in Fig. 12. These two results seem to contradict each other. In the typical Kondo semimetal, CeNiSn, although the SdH oscillation is observed in a good-quality sample [64], the ground state is rapidly changed to the semiconducting state by a small amount of doping [65]. We note that the SdH oscillation is observed also in $Ce_{0.95}La_{0.05}Ru_2Al_{10}$ exhibiting the increase of ρ below T_{min}.

Figures 18(a-1) and 18(b-1) show the magnetoresistance of $Ce_{0.9}La_{0.1}Ru_2Al_{10}$ and $Ce_{0.5}La_{0.5}Ru_2Al_{10}$ for $H \parallel b$, respectively. In both samples, a spin-flop transition from $m_{AF} \parallel b$ to $\parallel c$ appears at the magnetic field shown by the arrows. For the other field directions, no anomaly is seen up to 14.5 T, while they are not shown here. Figures 18(a-2) and 18(b-2) show the magnetic phase diagrams of these samples for $H \parallel a$. We note that the magnitude of ρ is smaller in the AFM phase with $m_{AF} \parallel c$ than that with $m_{AF} \parallel b$ as in $Ce_{1-x}Pr_xRu_2Al_{10}$ shown in Figs. 13.

Figure 19 shows the x dependence of H_{sf} of $Ce_{1-x}La_xRu_2Al_{10}$. The AFM order with $m_{AF} \parallel c$ is suppressed by La doping and for $x > 0.07$, the AFM order with $m_{AF} \parallel b$ is stable. The critical x_c^{sr} value of ~0.07 is over two times larger than $x_c^{sr} \sim 0.03$ in $Ce_{1-x}Pr_xRu_2Al_{10}$. The critical x_c value of ~0.6 where the AFM order disappears is also much larger than ~0.4 in $Ce_{1-x}Pr_xRu_2Al_{10}$.

2. *Magnetic susceptibility*

Figures 20(a) and 20(b) show the temperature dependence of the magnetic susceptibility of $Ce_{0.5}La_{0.5}Ru_2Al_{10}$ and

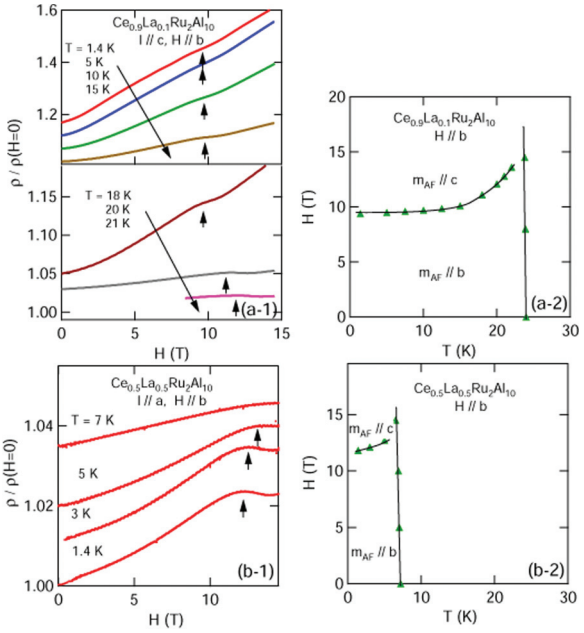

FIG. 18. (Color online) Magnetoresistance of (a-1) $Ce_{0.9}La_{0.1}Ru_2Al_{10}$ for $I \parallel c$ and $H \parallel b$ and (b-1) $Ce_{0.5}La_{0.5}Ru_2Al_{10}$ for $I \parallel a$ and $H \parallel b$. Magnetic phase diagram of (a-2) $Ce_{0.9}La_{0.1}Ru_2Al_{10}$ for $H \parallel b$ and (b-2) $Ce_{0.5}La_{0.5}Ru_2Al_{10}$ for $H \parallel b$.

$Ce_{0.3}La_{0.7}Ru_2Al_{10}$, respectively. Although the χ's of both samples along the three crystal axes show a similar temperature dependence above ~50 K, a large difference appears below ~20 K. In the latter, the magnetic order does not exist down to $T = 0$ K and the Curie-like increase is seen with decreasing temperature for all the magnetic field directions. In the former, T_0 is estimated to be ~7 K from the specific heat and electrical resistivity. The long-range order below 5 K in $Ce_{0.5}La_{0.5}Ru_2Al_{10}$ was recently confirmed through the μSR experiment [40]. The temperature dependence of χ_b and χ_c is weak below ~20 K. Very small temperature dependence of χ_b is consistent with the AFM order with $m_{AF} \parallel b$ expected from

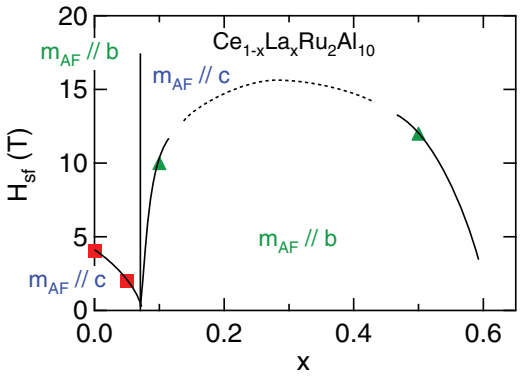

FIG. 19. (Color online) x dependence of the spin-flop transition field H_{sf} of $Ce_{1-x}La_xRu_2Al_{10}$. For $x < 0.07$, a spin-flop transition from $m_{AF} \parallel c$ to $\parallel b$ and for $x > 0.07$, that from $m_{AF} \parallel b$ to $\parallel c$. The dotted line is the conjectured x dependence of H_{sf}. The solid vertical line at $x \sim 0.07$ is the boundary where the magnetic anisotropy in the bc plane is changed.

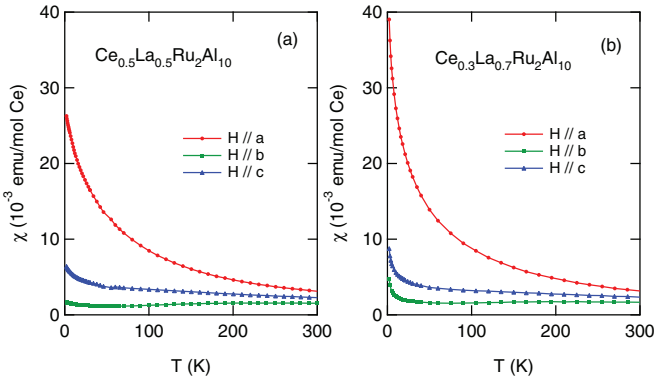

FIG. 20. (Color online) Temperature dependence of the magnetic susceptibility of (a-1) $Ce_{0.5}La_{0.5}Ru_2Al_{10}$ and (b-1) $Ce_{0.3}La_{0.7}Ru_2Al_{10}$. (a-2) and (b-2) show those for $H \parallel b$ and c below 100 K.

the magnetic phase diagram for $H \parallel b$. The increase of χ_a of $Ce_{0.5}La_{0.5}Ru_2Al_{10}$ at low temperatures is consistent with the magnetoresistance for $H \parallel a$, where the Ce ion has a rather free-ion-like nature in this sample.

3. *Lattice constants*

Figures 21(a)–21(d) show the x dependence of the lattice constants, the a, b, and c axes of $Ce_{1-x}La_xRu_2Al_{10}$ normalized by those of $LaRu_2Al_{10}$, respectively. The x dependence of the b axis is small but those of the a and c axes are large. This originates from the anisotropic c-f hybridization, which induces the larger contraction in the ac plane than along the b axis. The lattice constants do not obey the simple Vegard's law drawn by dashed lines in Fig. 21(d). In a close region to $CeRu_2Al_{10}$, the x dependence of the lattice constants is small and in a close region to $LaRu_2Al_{10}$, the lattice constants decrease roughly linearly to x and the slope is changed around $x \sim 0.7$.

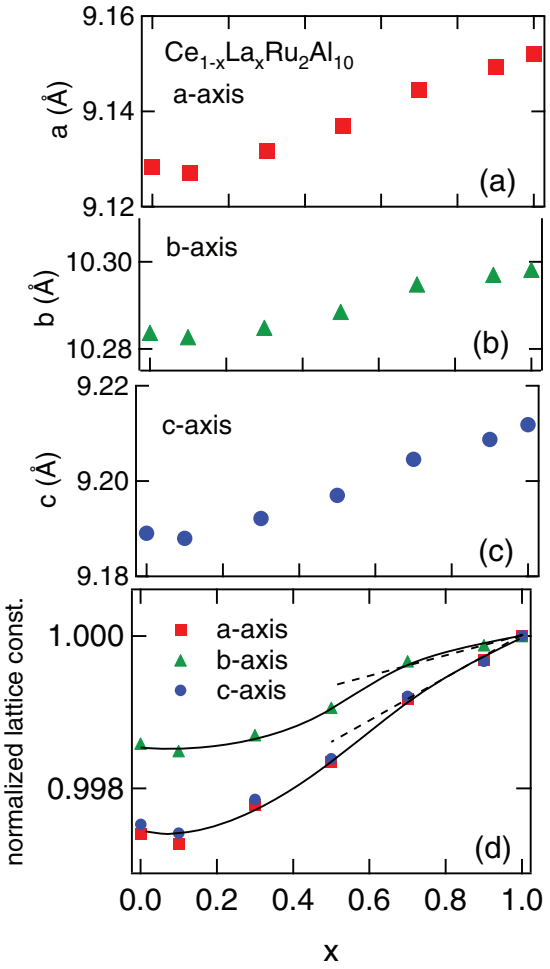

FIG. 21. (Color online) (a)–(c) x dependence of the lattice constants (a, b, and c axis) of $Ce_{1-x}La_xRu_2Al_{10}$ at room temperature, respectively. (d) These normalized by the lattice constants of $LaRu_2Al_{10}$. Solid lines are a guide to the eyes. Dashed lines follow Vegard's law.

IV. DISCUSSION

A. Magnetic properties

First, we discuss the Pr- and La-doping effects on the AFM order in $CeRu_2Al_{10}$. The important result in the present study is that the AFM order with $m_{AF} \parallel a$ never appears up to x_c. When T_0 is low in a large-x region close to x_c, the Ce-Ce interaction is weak and the single-ion magnetic anisotropy is expected to be dominant to determine the magnetization easy axis in the AFM phase. Then, the AFM order with $m_{AF} \parallel a$ is expected. However, the AFM order with $m_{AF} \parallel b$ is realized. This indicates that even in samples with such a low T_0, there should exist some interaction which avoids m_{AF} to align along the a axis. In $CeRu_2Al_{10}$, we proposed that this interaction is the strong c-f hybridization along the a axis [16,30,56]. The present results strongly suggest that this anisotropic c-f hybridization plays an important role even in the samples with a low T_0. Here, we should note that the x dependence of the lattice constants does not obey Vegard's law above $x \sim 0.7$ in $Ce_{1-x}La_xRu_2Al_{10}$. In a large-x region close to $LaRu_2Al_{10}$, a single-ion nature of the Ce ion should be dominant, where the lattice constants obey Vegard's law. The deviation from Vegard's law indicates that the contribution of the c-f hybridization is enhanced with increasing Ce concentration. $x \sim 0.7$ could be considered as the boundary between the Kondo semiconducting state and the impurity Kondo state. We note that it was reported that the spin gap exists at least up to $x = 0.3$ in $Ce_{1-x}La_xRu_2Al_{10}$ [47]. Then, we expect that the spin gap continues to exist up to x_c and the origin of the spin gap is the strong c-f hybridization along the a axis.

Next, we discuss the rotation of m_{AF} from c to b axis by a small Ce-site substitution at x^{sr}. Previously, in $Ce_{1-x}La_xRu_2Al_{10}$, we proposed that the origin of the rotation is the reduction of the c-f hybridization originating from the negative chemical pressure induced by La doping, whose ionic radius is larger than that in Ce [13]. However, the present results clearly indicate that this is not correct because the same type of the rotation of m_{AF} appears also in Pr doping, which induces the positive chemical pressure. On the other hand, there exists the following important relation between the rotation of m_{AF} and pressure effect. In $Ce_{1-x}La_xRu_2Al_{10}$ with $m_{AF} \parallel b$, m_{AF} is easily rotated to the c axis by applying a small pressure [32]. This clearly indicates that the c-f hybridization

dominates the magnetic anisotropy in the bc plane. Thereby, now, we conclude that the origin of the rotation of m_{AF} from c to b axis is the reduction of the c-f hybridization as a result of the decrease of the $4f$ electrons on Ce sites by Ce-site substitution. Here, we should note that the rotation of m_{AF} appears in a small-x region. Considering that such a small doping induces the rotation of m_{AF} in all the Ce sites, this change of the magnetization easy axis could not be ascribed to the single-ion effect but should be ascribed to the mechanism such as a coherence effect, which affects all the moments on Ce sites in the crystal. Namely, the anisotropic bandlike mechanism originating from the enhancement of the anisotropic c-f hybridization with increasing Ce concentration is associated with the magnetization easy axis in the AFM phase, although the microscopic mechanism is not known. The chemical pressure effect induced by Ce-site substitution is not effective to modify the strength of the c-f hybridization, because it may be due to the local effect but not the bandlike effect. We note that just at x_c^{sr}, there exists no magnetic anisotropy in the bc plane, where the Heisenberg model might be applicable. There, the anisotropic AFM exchange interaction just competes with the anisotropic c-f hybridization with maintaining the high T_0.

Finally, we briefly comment about the magnetic anisotropy in Re 3% doped $CeOs_2Al_{10}$ and $CeRu_2Al_{10}$. The neutron diffraction experiments indicate that in the former, $m_{AF} \parallel c$ and in the latter, $m_{AF} \parallel b$ [39]. By Re doping, the system is considered to move to the valence fluctuation regime. Then, we expect that the enhancement of the c-f hybridization by Re doping is rather isotropic and the anisotropy of the c-f hybridization is maintained. As the anisotropy in the bc plane is very small, a subtle change of the anisotropy in the bc plane determines the direction of m_{AF}. This could give rise to the different Re-doping effect on the magnetic anisotropy in the bc plane between $CeOs_2Al_{10}$ and $CeRu_2Al_{10}$.

B. Transport properties

The electrical resistivity under the transverse magnetic field shows quite different magnetic field effects below and above T_0. It is quite small above T_0 but is very large below T_0. The magnitude of the Hall resistivity ρ_H is also very different below and above T_0; i.e., it is very small above T_0 and very large below T_0 [54]. These strongly suggest that such large differences of ρ and ρ_H below and above T_0 originate from the different size of the Fermi surface below and above T_0. It is large above T_0 but is small below T_0.

The increase of ρ_0 below T_0 gives important information on the Fermi surface below T_0. ρ of $CeRu_2Al_{10}$ shows the increase below T_0 and after taking a maximum at T_{max}, it decreases with decreasing temperature. The increase of T_0 originates from the AFM order and this increase is seen for all the current directions, which is difficult to explain by the superzone gap formed by the AFM order. In a normal AFM compound, the Fermi surface is cut anisotropically below T_N and the anisotropic superzone gap opens below T_N. Then, the anisotropic increase of ρ is expected below T_N. In fact, in the localized antiferromagnet, $NdFe_2Al_{10}$, such an anisotropic behavior is clearly observed. The magnetic structure of this compound was recently determined, where $k_1 = (0\frac{3}{4}0)$ and $k_2 = (0\frac{1}{4}0)$ are the ordering vectors [66]. Due to this type of AFM order, the increase of ρ below T_N for $I \parallel b$ is expected but not for $I \parallel a$ and c. Our recent results of ρ in $NdFe_2Al_{10}$ showed that the large increase is seen only for $I \parallel b$ but a decrease for $I \parallel a$ and c below T_N [67]. This anisotropic resistivity below T_N is consistent with the AFM order in $NdFe_2Al_{10}$. On the other hand, in CeT_2Al_{10}, the increase below T_0 is seen for all the current directions. This indicates that the gap is opened on almost the area of the large Fermi surfaces by the AFM order and the small Fermi surfaces are constructed below T_0. Such a gap opening on the Fermi surface is different from that in the normal AFM compound and may indicate the characteristic of the AFM order in the Kondo semiconductor. The microscopic mechanism should be clarified in the future.

Next, we discuss the anisotropic behavior of ρ below T_0 in $Ce_{1-x}Ln_xRu_2Al_{10}$ (Ln=La, Pr). In principle, the temperature dependence of ρ below T_0 originates from two different kinds of contributions. One is the increase due to the opening of the charge gap and the other is the decrease due to the suppression of the magnetic scattering, although in a real system, both could be associated with each other. The small Fermi surfaces are formed by the AFM order below T_0. The small Fermi surface is generally isotropic and the increase of ρ below T_0 is expected to be isotropic. Then, the anisotropy of ρ below T_0 is expected to originate from the anisotropic magnetic scattering. ρ of $CeRu_2Al_{10}$ and $CeOs_2Al_{10}$ show the anisotropic increase below T_0. It is large for $I \parallel b$ and $\parallel c$ but is small for $I \parallel a$ [13,37]. This anisotropy is maintained also by Pr or La doping. The small increase of ρ below T_0 for $I \parallel a$ suggests the largest suppression of the magnetic scattering for $I \parallel a$. With increasing x in $Ce_{1-x}Ln_xRu_2Al_{10}$ (Ln=La, Pr), the separation between T_{max} and T_0 is reduced for $I \parallel a$, but not for $I \parallel b$ and c. This also suggests the largest suppression of the magnetic scattering for $I \parallel a$. This is supported by the largest decrease of ρ below T_{max} for $I \parallel a$ and the smallest one for $I \parallel b$ in $Ce_{1-x}Pr_xRu_2Al_{10}$ as is seen in Figs. 8–10. This anisotropic decrease of ρ below T_{max} indicates the anisotropic magnetic scattering below T_0. Here, we propose that the opening of the anisotropic spin gap induced by the anisotropic c-f hybridization reduces the magnetic scattering anisotropically.

Finally, we briefly comment on the difference between the present system and Kondo semimetal CeNiSn with the nonmagnetic ground state [64]. Both compounds exhibit SdH oscillations. In the latter, the SdH frequency of $\sim$100 T was observed and the effective mass is $\sim 10m_e$, which is large for a small Fermi surface. In $CeRu_2Al_{10}$, the small SdH frequency of $\sim$20 $\sim$ 100 T was observed [60,62] but its effective mass of $\sim 1m_e$ is much smaller than that in CeNiSn. In both compounds, the transport properties are dominated by the small Fermi surfaces. These differences might be associated with the difference of the ground state between the AFM- and nonmagnetic-Kondo semiconductors, where the mechanism to construct the small Fermi surface is also different.

V. CONCLUSION

We have studied Pr- and La-doping effects on the magnetic anisotropy in the AFM phase of $CeRu_2Al_{10}$. χ of $PrRu_2Al_{10}$ exhibits a large anisotropy below room temperature and the

overall CEF splitting with a singlet ground state is estimated to be ~800 K from the analysis using the CEF Hamiltonian. The origin of such a high CEF splitting is not known and further studies are necessary. In $Ce_{1-x}Pr_xRu_2Al_{10}$, the CEF level scheme of the Pr ion is not changed with x, indicating the single-ion nature of the doped Pr ion. m_{AF} is rotated from c to b axis at $x_c^{sr} \sim 0.03$ in $Ce_{1-x}Pr_xRu_2Al_{10}$ as was observed in $Ce_{1-x}La_xRu_2Al_{10}$, where the rotation of m_{AF} appears at $x_c^{sr} \sim 0.07$. As the ionic radius of La is larger than that of Ce and that of Pr is smaller than that of Ce, these results indicate that the rotation of m_{AF} from c to b axis is not associated with the chemical pressure effect, but it is caused by the reduction of the c-f hybridization originating from the decrease of $4f$ electrons of Ce ions by the Ce-site substitution. Since a small amount of Ce-site substitution rotates the magnetic moments of all the Ce ions, the magnetic anisotropy does not originate from the local single ion effect but from the bandlike effect through the anisotropic c-f hybridization. The AFM order exists up to $x_c \sim 0.4$ in $Ce_{1-x}Pr_xRu_2Al_{10}$ and $x_c \sim 0.6$ in $Ce_{1-x}La_xRu_2Al_{10}$. The magnetic phase diagrams of $Ce_{1-x}Pr_xRu_2Al_{10}$ and $Ce_{1-x}La_xRu_2Al_{10}$ indicate that for $x > x_c^{sr}$, the AFM order with $m_{AF} \parallel b$ continues to exist up to x_c in both doping systems. This contradicts the simple expectation that the magnetization easy axis is dominated by the single-ion magnetic anisotropy along the a axis due to the weak Ce-Ce interaction. Even in the samples with a low T_0 near x_c, the anisotropic c-f hybridization dominates the AFM order. The large positive transverse magnetoresistance is seen below T_0 but a very small one above T_0. The SdH oscillation was observed even in $Ce_{0.8}Pr_{0.2}Ru_2Al_{10}$. From these observations together with the results of Hall resistivity, we propose that there exist large Fermi surfaces above T_0 and small ones below T_0. The gap is opened by the AFM order on almost the area of the large Fermi surfaces and the small Fermi surfaces are constructed below T_0 by the unknown mechanism specific to the AFM order in Kondo semiconductors. With increasing Pr doping, the two-dimensional characteristic of the electrical resistivity becomes clearer. The largest suppression of the magnetic scattering below T_0 is observed for $I \parallel a$ and the smallest for $I \parallel b$. This anisotropy may be associated with the anisotropic c-f hybridization, which may contribute to the anisotropic magnetic scattering of the conduction electron below T_0.

[1] V. M. Thiede, T. Ebel, and W. Jeitsschko, J. Mater. Chem. **8**, 125 (1998).

[2] A. M. Strydom, Phys. B (Amsterdam, Neth.) **404**, 2981 (2009).

[3] T. Nishioka, Y. Kawamura, T. Takesaka, R. Kobayashi, H. Kato, M. Matsumura, K. Kodama, K. Matsubayashi, and Y. Uwatoko, J. Phys. Soc. Jpn. **78**, 123705 (2009).

[4] Y. Muro, J. Kajino, T. Onimaru, and T. Takabatake, J. Phys. Soc. Jpn. **80**, SA021 (2011).

[5] M. Sera, H. Nohara, M. Nakamura, H. Tanida, T. Nishioka, and M. Matsumura, Phys. Rev. B **88**, 100404(R) (2013).

[6] S. Kimura, T. Iizuka, H. Miyazaki, T. Hajiri, M. Matsunami, T. Mori, A. Irizawa, Y. Muro, J. Kajino, and T. Takabatake, Phys. Rev. B **84**, 165125 (2011).

[7] M. Samsel-Czekala, E. Talik, M. Pasturel, and R. Troc, J. Alloys Compd. **554**, 438 (2013).

[8] T. Ishiga, T. Wakita, R. Yoshida, H. Okazaki, K. Tsubota, M. Sunagawa, K. Uenaka, K. Okada, H. Kumigashira, M. Oshima, K. Yutani, Y. Muro, T. Takabatake, Y. Muraoka, and T. Yokoya, J. Phys. Soc. Jpn. **83**, 094717 (2014).

[9] Y. Zekko, Y. Yamamoto, H. Yamaoka, F. Tajima, T. Nishioka, F. Strigari, A. Severing, J-F. Lin, N. Hiraoka, H. Ishii, K-D. Tsuei, and J. Mizuki, Phys. Rev. B **89**, 125108 (2014).

[10] F. Strigari, M. Sundermann, Y. Muro, K. Yutani, T. Takabatake, K.-D. Tsuei, Y. F. Liao, A. Tanaka, P. Thalmeier, M. W. Haverkort, L. H. Tjeng, and A. Severing, J. Electron Spectrosc. Relat. Phenom. **199**, 56 (2015).

[11] Y. Muro, K. Motoya, Y. Saiga, and T. Takabatake, J. Phys. Soc. Jpn. **78**, 083707 (2009).

[12] K. Umeo, T. Ohsuka, Y. Muro, J. Kajino, and T. Takabatake, J. Phys. Soc. Jpn. **80**, 064709 (2011).

[13] H. Tanida, Y. Nonaka, D. Tanaka, M. Sera, T. Nishioka, and M. Matsumura, Phys. Rev. B **86**, 085144 (2012).

[14] H. Tanida, M. Nakamura, M. Sera, A. Kondo, K. Kindo, T. Nishioka, and M. Matsumura, J. Phys. Soc. Jpn. **83**, 084708 (2014).

[15] H. Tanida, D. Tanaka, M. Sera, C. Moriyoshi, Y. Kuroiwa, T. Takesaka, T. Nishioka, H. Kato, and M. Matsumura, J. Phys. Soc. Jpn. **79**, 043708 (2010).

[16] A. Kondo, J. Wang, K. Kindo, Y. Ogane, Y. Kawamura, S. Tanimoto, T. Nishioka, D. Tanaka, H. Tanida, and M. Sera, Phys. Rev. B **83**, 180415(R) (2011).

[17] H. Tanida, H. Nohara, M. Sera, T. Nishioka, M. Matsumura, and R. Kobayashi, Phys. Rev. B **90**, 165124 (2014).

[18] K. Hanzawa, J. Phys. Soc. Jpn. **79**, 043710 (2010).

[19] S. Hoshino and Y. Kuramoto, Phys. Rev. Lett. **111**, 026401 (2013).

[20] T. Kikuchi, S. Hoshino, and Y. Kuramoto, J. Phys. Soc. Jpn. **83**, 114706 (2014).

[21] S. Kambe, H. Chudo, Y. Tokunaga, T. Koyama, H. Sakai, T. U. Ito, K. Ninomiya, W. Higemoto, T. Takesaka, T. Nishioka, and Y. Miyake, J. Phys. Soc. Jpn. **79**, 053708 (2010).

[22] D. D. Khalyavin, A. D. Hillier, D. T. Adroja, A. M. Strydom, P. Manuel, L. C. Chapon, P. Peratheepan, K. Knight, P. Deen, C. Ritter, Y. Muro, and T. Takabatake, Phys. Rev. B **82**, 100405 (2010).

[23] J-M. Mignot, J. Robert, G. Andre, A. M. Bataille, T. Nishioka, R. Kobayashi, M. Matsumura, H. Tanida, D. Tanaka, and M. Sera, J. Phys. Soc. Jpn. **80**, SA022 (2011).

[24] H. Kato, R. Kobayashi, T. Takesaka, T. Nishioka, M. Matsumura, K. Kaneko, and N. Metoki, J. Phys. Soc. Jpn. **80**, 073701 (2011).

[25] M. Matsumura, Y. Kawamura, S. Edamoto, T. Takesaka, H. Kato, T. Nishioka, Y. Tokunaga, S. Kambe, and H. Yasuoka, J. Phys. Soc. Jpn. **78**, 123713 (2009).

[26] M. Matsumura, H. Tanida, D. Tanaka, H. Kato, T. Nishioka, and M. Sera, J. Phys. Soc. Jpn. **80**, 085001 (2011).

[27] H. Tanida, D. Tanaka, M. Sera, C. Moriyoshi, Y. Kuroiwa, T. Takesaka, T. Nishioka, H. Kato, and M. Matsumura, J. Phys. Soc. Jpn. **79**, 083701 (2010).
[28] H. Muro, J. Kajino, K. Umeo, K. Nishimoto, R. Tamura, and T. Takabatake, Phys. Rev. B **81**, 214401 (2010).
[29] A. Kondo, J. Wang, K. Kindo, T. Takesaka, Y. Kawwamura, T. Nishioka, D. Tanaka, H. Tanida, and M. Sera, J. Phys. Soc. Jpn. **79**, 073709 (2010).
[30] H. Tanida, D. Tanaka, Y. Nonaka, M. Sera, M. Matsumura, and T. Nishioka, Phys. Rev. B **84**, 233202 (2011).
[31] K. Kunimori, M. Nakamura, H. Nohara, H. Tanida, M. Sera, T. Nishioka, and M. Matsumura, Phys. Rev. B **86**, 245106 (2012).
[32] H. Tanida, D. Tanaka, Y. Nonaka, S. Kobayashi, M. Sera, T. Nishioka, and M. Matsumura, Phys. Rev. B **88**, 045135 (2013).
[33] A. Kondo, K. Kindo, K. Kunimori, H. Nohara, H. Tanida, M. Sera, R. Kobayashi, T. Nishioka, and M. Matsumura, J. Phys. Soc. Jpn. **82**, 054709 (2013).
[34] H. Guo, H. Tanida, R. Kobayashi, I. Kawasaki, M. Sera, T. Nishioka, M. Matsumura, I. Watanabe, and Z. A. Xu, Phys. Rev. B **88**, 115206 (2013).
[35] R. Kobayashi, Y. Ogane, D. Hirai, T. Nishioka, M. Matsumura, Y. Kawamura, K. Matsubayashi, Y. Uwatoko, H. Tanida, and M. Sera, J. Phys. Soc. Jpn. **82**, 093702 (2013).
[36] R. Kobayashi, K. Kaneko, K. Saito, J-M. Mignot, G. Andre, J. Robert, S. Wakimoto, M. Matsuda, S. Chi, Y. Haga, T. D. Matsuda, E. Yamamoto, T. Nishioka, M. Matsumura, H. Tanida, and M. Sera, J. Phys. Soc. Jpn. **83**, 104707 (2014).
[37] J. Kawabata, T. Takabatake, K. Umeo, and Y. Muro, Phys. Rev. B **89**, 094404 (2014).
[38] D. D. Khalyavin, D. T. Adroja, P. Manuel, J. Kawabata, K. Umeo, T. Takabatake, and A. M. Strydom, Phys. Rev. B **88**, 060403(R) (2013).
[39] A. Bhattacharyya, D. D. Khalyavin, D. T. Adroja, A. M. Strydom, A. D. Hillier, P. Manuel, T. Takabatake, J. W. Taylor, and C. Ritter, Phys. Rev. B **90**, 174412 (2014).
[40] D. T. Adroja, A. D. Hiller, C. Ritter, A. Bhattacharyya, D. D. Khalyavin, A. M. Strydom, P. Peratheepan, B. Bak, M. M. Koza, J. Kawabata, Y. Yamada, Y. Okada, Y. Muro, T. Takabatake, and J. W. Taylor, arXiv:1501.07497.
[41] J. Robert, J-M. Mignot, G. Andre, T. Nishioka, R. Kobayashi, M. Matsumura, H. Tanida, D. Tanaka, and M. Sera, Phys. Rev. B **82**, 100404(R) (2010).
[42] D. T. Adroja, A. D. Hillier, P. P. Deen, A. M. Strydom, Y. Muro, J. Kajino, W. A. Kockelmann, T. Takabatake, V. K. Anand, J. R. Stewart, and J. Taylor, Phys. Rev. B **82**, 104405 (2010).
[43] J. Robert, J-M. Mignot, S. Petit, P. Steffens, T. Nishioka, R. Kobayashi, M. Matsumura, H. Tanida, D. Tanaka, and M. Sera, Phys. Rev. Lett. **109**, 267208 (2012).
[44] D. T. Adroja, A. D. Hillier, Y. Muro, J. Kajino, T. Takabatake, P. Peratheepan, A. M. Strydom, P. P. Deen, F. Demmel, J. R. Stewart, J. W. Taylor, R. I. Smith, S. Ramos, and M. A. Adams, Phys. Rev. B **87**, 224415 (2013).
[45] J-M. Mignot, P. A. Alekseev, J. Robert, S. Petit, T. Nishioka, M. Matsumura, R. Kobayashi, H. Tanida, H. Nohara, and M. Sera, Phys. Rev. B **89**, 161103(R) (2014).
[46] D. T. Adroja, A. D. Hikker, Y. Muro, T. Takabatake, A. M. Strydom, A. Bhattacharyya, A. Daoud-Aladin, and J. W. Taylor, Phys. Scr. **88**, 068505 (2013).
[47] D. T. Adroja, A. D. Hiller. P. Peratheepan, A. M. Strydom, Y. Muro, J. R. Stewart, J. Taylor, F. Demmel, P. P. Deen, and T. Takabatake, abstracts in SCES2011 conference, http://www.the-conference.com.conferences/2011/sces2011/abstracts/original PDFs/1401.pdf.
[48] C. S. Lue, S. H. Yang, A. C. Abhyankar, Y. D. Hsu, H. T. Hong, and Y. K. Kuo, Phys. Rev. B **82**, 045111 (2010).
[49] Y. Kawamura, S. Edamoto, T. Takesaka, T. Nishioka, H. Kato, M. Matsumura, Y. Tokunaga, S. Kambe, and H. Yasuoka, J. Phys. Soc. Jpn. **79**, 103701 (2010).
[50] M. Matsumura, N. Tomita, S. Yanimoto, Y. Kawamura, R. Kobayashi, H. Kato, T. Nishioka, H. Tanida, and M. Sera, J. Phys. Soc. Jpn. **82**, 023702 (2013).
[51] M. Matsumura, N. Tomita, J. Matsuoka, Y. Kishimoto, H. Kato, K. Kitagawa, T. Nishioka, H. Tanida, and M. Sera, J. Phys. Soc. Jpn. **83**, 103705 (2014).
[52] S. Kimura, T. Iizuka, H. Miyazaki, A. Irizawa, Y. Muro, and T. Takabatake, Phys. Rev. Lett. **106**, 056404 (2011).
[53] S. Kimura, Y. Muro, and T. Takabatake, J. Phys. Soc. Jpn. **80**, 033702 (2011).
[54] H. Tanida, D. Tanaka, M. Sera, C. Moriyoshi, Y. Kuroiwa, T. Takesaka, T. Nishioka, H. Kato, and M. Matsumura, J. Phys. Soc. Jpn. **79**, 063709 (2010).
[55] H. Tanida, D. Tanaka, M. Sera, S. Tanimoto, T. Nishioka, M. Matsumura, M. Ogawa, C. Moriyoshi, Y. Kuroiwa, J. E. Kim, N. Tsuji, and M. Takata, Phys. Rev. B **84**, 115128 (2011).
[56] M. Sera, D. Tanaka, H. Tanida, C. Moriyoshi, M. Ogawa, Y. Kuroiwa, T. Nishioka, M. Matsumura, J. Kim, N. Tsuji, and M. Takata, J. Phys. Soc. Jpn. **82**, 024603 (2013).
[57] F. Strigari, T. Willers, Y. Muro, K. Yutani, T. Takabatake, Z. Hu, Y.-Y. Chin, S. Agrestini, H.-J. Lin, C. T. Chen, A. Tanaka, M. W. Haverkort, L. H. Tjeng, and A. Severing, Phys. Rev. B **86**, 081105(R) (2012).
[58] F. Strigari, T. Willers, Y. Muro, K. Yutani, T. Takabatake, Z. Hu, S. Agrestini, C.-Y. Kuo, Y.-Y. Chin, H.-J. Lin, T. W. Pi, C. T. Chen, E. Weschke, E. Schierle, A. Tanaka, M. W. Haverkort, L. H. Tjeng, and A. Severing, Phys. Rev. B **87**, 125119 (2013).
[59] K. Nagano, T. Hasegawa, N. Ogita, M. Udagawa, H. Tanida, H. Nohara, M. Nakamura, M. Sera, T. Nishioka, and M. Matsumura, J. Phys. Soc. Jpn. Conf. Proc. **3**, 011070 (2014).
[60] A. Kondo, J. Wang, K. Kindo, T. Takesaka, Y. Ogane, Y. Kawasaki, T. Nishioka, D. Tanaka, H. Tanida, and M. Sera, J. Phys. Soc. Jpn. **80**, 013701 (2011).
[61] M. Sakoda, S. Tanaka, E. Matsuoka, H. Sugawara, H. Harima, F. Honda, R. Settai, Y. Onuki, T. D. Matsuda, and Y. Haga, J. Phys. Soc. Jpn. **80**, 084716 (2011).
[62] M. Sakoda, T. Nishiwaki, E. Matsuoka, H. Harima, H. Tanida, M. Sera, and H. Sugawara, J. Phys. Soc. Jpn. Conf. Proc. **3**, 011043 (2014).
[63] G. Morrison, N. Haldoaarchchige, D. Young, and J. Y. Chan, J. Phys.: Condens. Matter **24**, 356002 (2012).
[64] T. Terashima, C. Terakura, S. Uji, H. Aoki, Y. Echizen, and T. Takabatake, Phys. Rev. B **66**, 075127 (2002).
[65] T. Takabatake, Y. Echizen, T. Yoshino, K. Kobayashi, G. Nakamoto, H. Fujii, and M. Sera, Phys. Rev. B **59**, 13878 (1999).
[66] J. Robert, F. Damay, K. Saito, A. M. Bataille, F. Porcher, G. Andre, A. Gukasov, J-M. Mignot, H. Tanida, and M. Sera, Phys. Rev. B **90**, 224425 (2014).
[67] H. Tanida *et al.* (unpublished).